



## Discovery of a Three-Dimensional Topological Dirac Semimetal, Na<sub>3</sub>Bi

Z. K. Liu *et al.*

*Science* **343**, 864 (2014);

DOI: 10.1126/science.1245085

*This copy is for your personal, non-commercial use only.*

If you wish to distribute this article to others, you can order high-quality copies for your colleagues, clients, or customers by [clicking here](#).

Permission to republish or repurpose articles or portions of articles can be obtained by following the guidelines [here](#).

**The following resources related to this article are available online at [www.sciencemag.org](http://www.sciencemag.org) (this information is current as of March 14, 2014 ):**

**Updated information and services**, including high-resolution figures, can be found in the online version of this article at:

<http://www.sciencemag.org/content/343/6173/864.full.html>

**Supporting Online Material** can be found at:

<http://www.sciencemag.org/content/suppl/2014/01/15/science.1245085.DC1.html>

This article **cites 34 articles**, 2 of which can be accessed free:

<http://www.sciencemag.org/content/343/6173/864.full.html#ref-list-1>

This article appears in the following **subject collections**:

Physics

<http://www.sciencemag.org/cgi/collection/physics>

# Discovery of a Three-Dimensional Topological Dirac Semimetal, $\text{Na}_3\text{Bi}$

Z. K. Liu,<sup>1\*</sup> B. Zhou,<sup>2,3\*</sup> Y. Zhang,<sup>3</sup> Z. J. Wang,<sup>4</sup> H. M. Weng,<sup>4,5</sup> D. Prabhakaran,<sup>2</sup> S.-K. Mo,<sup>3</sup> Z. X. Shen,<sup>1</sup> Z. Fang,<sup>4,5</sup> X. Dai,<sup>4,5</sup> Z. Hussain,<sup>3</sup> Y. L. Chen<sup>2,6†</sup>

Three-dimensional (3D) topological Dirac semimetals (TDSs) represent an unusual state of quantum matter that can be viewed as “3D graphene.” In contrast to 2D Dirac fermions in graphene or on the surface of 3D topological insulators, TDSs possess 3D Dirac fermions in the bulk. By investigating the electronic structure of  $\text{Na}_3\text{Bi}$  with angle-resolved photoemission spectroscopy, we detected 3D Dirac fermions with linear dispersions along all momentum directions. Furthermore, we demonstrated the robustness of 3D Dirac fermions in  $\text{Na}_3\text{Bi}$  against in situ surface doping. Our results establish  $\text{Na}_3\text{Bi}$  as a model system for 3D TDSs, which can serve as an ideal platform for the systematic study of quantum phase transitions between rich topological quantum states.

The discoveries of graphene and topological insulators (TIs) have inspired enormous efforts in the search for materials with similar electronic and topological properties (1–4). Graphene, a single sheet of carbon atoms, hosts two-dimensional (2D) Dirac fermions in its electronic structure (1, 2, 5); TIs are materials with a bulk energy gap but gapless surface states formed by an odd number of Dirac fermions with

helical spin texture (3, 4, 6–8). In the course of this search, the following questions arose: Does a 3D counterpart of graphene exist? Can materials other than insulators possess unusual topology in their electronic structures?

In a class of materials called the topological Dirac semimetals, both of these questions are answered in the affirmative. There, the bulk conduction and valence bands touch only at dis-

crete (Dirac) points and disperse linearly along all (three) momentum directions, forming bulk (3D) Dirac fermions—a natural 3D counterpart of graphene. Although a similar electronic structure was discussed more than seven decades ago (9), its topological classification was only appreciated recently (10–15), leading to the theoretical proposal of topological Dirac semimetals (TDSs) (12–16).

The distinct electronic structure of a TDS not only makes it possible to realize some exciting phenomena and applications of graphene (17) in 3D materials—it also gives rise to many unusual properties, such as the giant diamagnetism that diverges logarithmically when the Fermi energy ( $E_F$ ) approaches the 3D Dirac point (16, 18, 19); quantum magnetoresistance showing linear field dependence in the bulk (20, 21); characteristic Landau level structures under a strong magnetic

<sup>1</sup>Stanford Institute for Materials and Energy Sciences, SLAC National Accelerator Laboratory, 2575 Sand Hill Road, Menlo Park, CA 94025, USA. <sup>2</sup>Physics Department, Clarendon Laboratory, University of Oxford, Parks Road, OX1 3PU, UK. <sup>3</sup>Advanced Light Source, Lawrence Berkeley National Laboratory, Berkeley, CA 94720, USA. <sup>4</sup>Beijing National Laboratory for Condensed Matter Physics and Institute of Physics, Chinese Academy of Sciences, Beijing 100190, China. <sup>5</sup>Collaborative Innovation Center of Quantum Matter, Beijing, China. <sup>6</sup>Diamond Light Source and Rutherford Appleton Laboratory, Didcot, UK.

\*These authors contributed equally to this work.

†Corresponding author. E-mail: yulin.chen@physics.ox.ac.uk

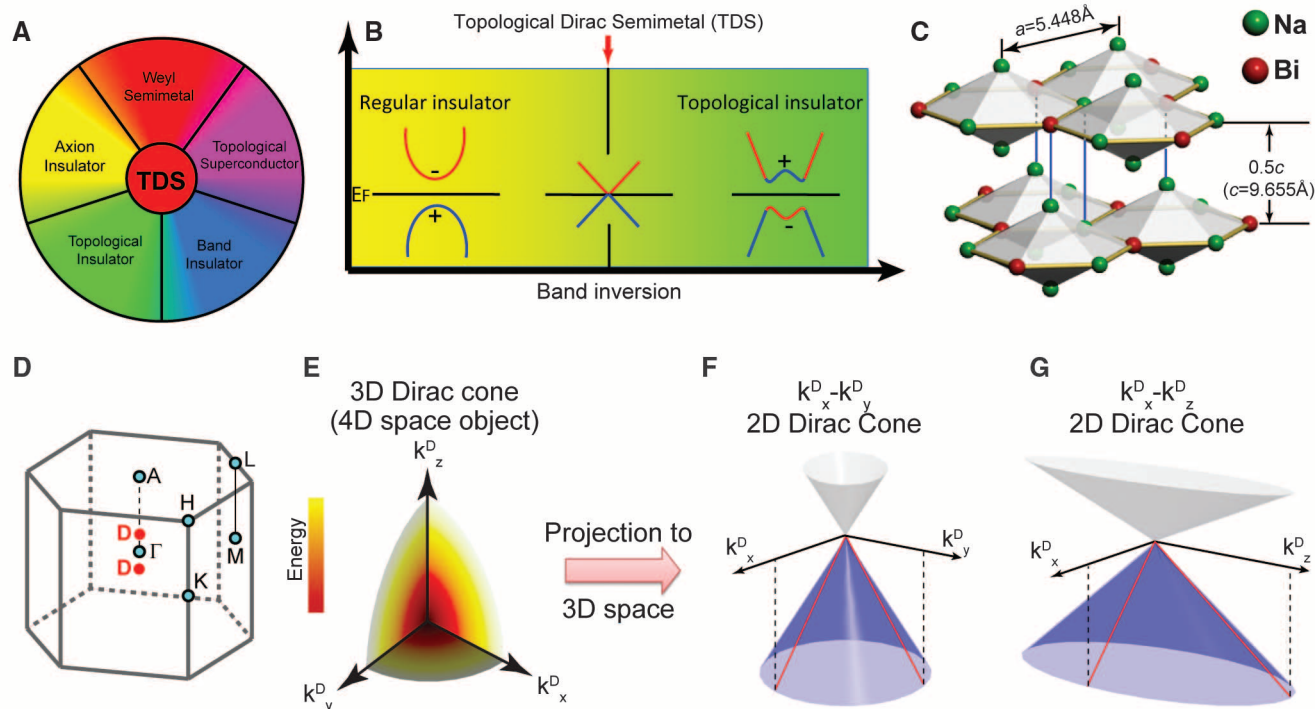


**Fig. 1. Basic characteristics of the TDS.** (A) The TDS state neighbors various unusual states. (B) The TDS state may be realized at the quantum critical point in the topological quantum phase transition from a normal insulator to a topological insulator. The “+” and “−” signs denote the even and odd parity of the bands at the time-reversal invariant point, respectively. (C) Crystal structure and (D) the BZ of  $\text{Na}_3\text{Bi}$ . Cyan dots

indicate the high-symmetry points of the BZ, and red dots highlight the 3D Dirac point positions. (E) Visualization of a 3D Dirac fermion dispersion ( $E = V_x \cdot k_x^D + V_y \cdot k_y^D + V_z \cdot k_z^D$ ); the color scale represents energy. (F and G) Projection of the 3D Dirac fermion onto ( $k_x^D, k_y^D, E$ ) and ( $k_x^D, k_z^D, E$ ) spaces (see text). Red lines outline the linear dispersions along  $k_x^D, k_y^D$ , and  $k_z^D$  directions.

field; and oscillating quantum spin Hall effect in quantum well structures (15, 22). The 3D Dirac fermion in a TDS is composed of two overlapping Weyl fermions (chiral massless particles previously studied extensively in high-energy physics—e.g., as a description of neutrinos) (23) that can be separated in the momentum space if time-reversal or inversion symmetry is broken. This would result in a topological Weyl semimetal, another novel topological quantum state that shows a distinct Fermi-arcs geometry (12, 24), exhibiting the pressure-induced anomalous Hall effect (25) and quantized anomalous Hall effect in quantum well structures (24).

In addition to these unusual properties, the TDS is the neighbor state to various quantum states (Fig. 1, A and B) (12–16, 26) ranging from regular band insulators to topological superconductors. This versatility makes the TDS an ideal parent compound for the realization of other novel states, as well as a platform for the systematic study of topological quantum phase transitions.

The physical realization of the TDS is, however, challenging. In principle, it may be realized through topological phase transitions, such as tuning chemical composition or spin-orbital cou-

pling strength to the quantum critical point through a normal insulator–topological insulator transition (Fig. 1B). Recently, it was realized that the crystal symmetry can protect and stabilize 3D Dirac points in several stoichiometric compounds such as  $\beta$ -cristobalite  $\text{BiO}_2$  (14) and  $\text{A}_3\text{Bi}$  (where A is Na, K, or Rb) family of compounds (15). Because of the metastable nature of  $\beta$ -cristobalite  $\text{BiO}_2$ , we chose to study  $\text{Na}_3\text{Bi}$ .

We performed angle-resolved photoemission spectroscopy (ARPES) measurements to investigate the electronic structures of  $\text{Na}_3\text{Bi}$  (001) single crystals. [Further details of the sample preparation and ARPES experiments are available in (27).] The crystal structure of  $\text{Na}_3\text{Bi}$  (Fig. 1C) is composed of stacked ...Na–(Na/Bi)–Na... triple-layer groups, with the adjacent triple layers rotated by  $60^\circ$  with respect to each other. The 3D Brillouin zone (BZ) of  $\text{Na}_3\text{Bi}$  is illustrated in Fig. 1D, with high-symmetry points indicated. According to recent ab initio calculations (15), a pair of 3D Dirac fermions is located near the  $\Gamma$  point in each BZ (labeled as “D” in Fig. 1D), with linear dispersion along  $k_x$ ,  $k_y$ , and  $k_z$  directions. Because a 3D Dirac fermion is a surface in 4D space ( $E = V_x \cdot k_x^D + V_y \cdot k_y^D + V_z \cdot k_z^D$ , where  $V_x$ ,  $V_y$ , and  $V_z$  are the Fermi velocities

along  $x$ ,  $y$ , and  $z$  directions, respectively; and  $k_x^D$ ,  $k_y^D$ , and  $k_z^D$  represent the momentum measured from the Dirac point), in Fig. 1E, we visualize it by using  $k_x^D$ ,  $k_y^D$ , and  $k_z^D$  as variables and colors to represent  $E$  (the fourth dimension). The projections of the 3D Dirac fermion onto two 2D momentum planes are shown in Fig. 1, F and G. The figures reflect the calculated small in-plane and large out-of-plane anisotropy ( $V_x \approx V_y = 3.74 \times 10^5$  m/s,  $V_z = 2.89 \times 10^4$  m/s).

The overall electronic structure from ARPES measurements is summarized in Fig. 2. The characteristic peaks of Na and Bi elements are evident in the core-level spectra (Fig. 2A); the band dispersions (Fig. 2B) agree well with our ab initio calculations, represented by solid lines [details of the calculations are in (27)]. The electronic structure at the Dirac point is illustrated in Fig. 2C, showing a cone shape with linear dispersions [details on selecting  $k_z$  positions and identifying Dirac points in momentum space are in (27)]. This Dirac cone dispersion results in a pointlike Fermi surface (FS) at  $\bar{\Gamma}$  in the projected 2D BZ (Fig. 2D). Moreover, the constant-energy contours of the Dirac cone at different binding energies (Fig. 2E) demonstrate the small in-plane anisotropy.

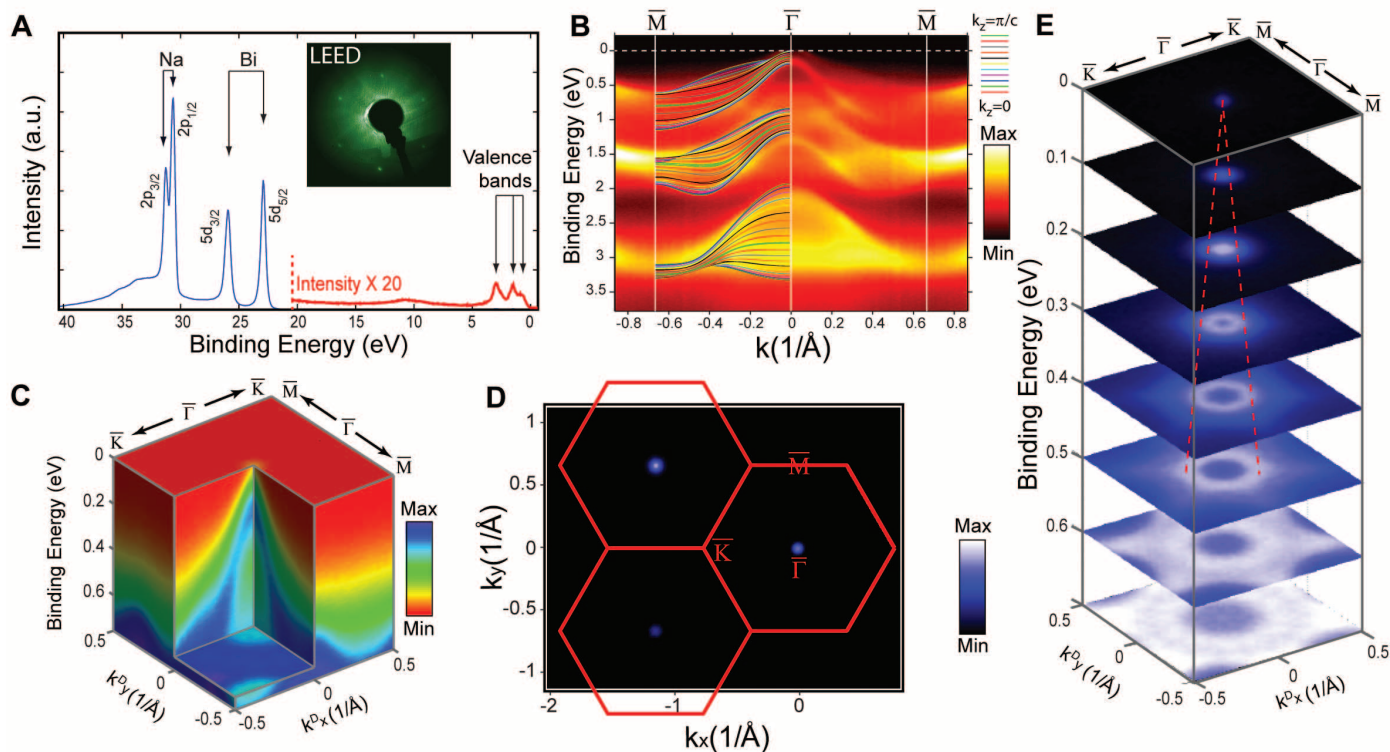


**Fig. 2. Electronic structure of  $\text{Na}_3\text{Bi}$ .** (A) Core-level photoemission spectrum shows strong characteristic Na 2p and Bi 5d doublet peaks (blue curve). Features at low binding energy ( $E_B < 21$  eV) were magnified 20 times to enhance the details (red curve). Inset: Low-energy electron diffraction (LEED) pattern shows the hexagonal structure of  $\text{Na}_3\text{Bi}$  (001) surface. (B) Comparison of the valence band spectra between ARPES measurement (background) and ab initio calculations (solid lines) along the  $\bar{M}-\bar{\Gamma}-\bar{M}$  direction. The color of the lines represents different  $k_z$  dispersions in the calculation.

(C) A 3D intensity plot of the photoemission spectra at the Dirac point, showing cone-shape dispersion. (D) Broad FS map from ARPES measurements that covers three BZs. The red hexagons represent the surface BZ, and the uneven intensity of the FS points of different BZs results from the matrix element effect. (E) Stacking plot of constant-energy contours at different binding energies shows Dirac cone band structure. Red dotted lines are guides to the eye that indicate the dispersions and intersect at the Dirac point.



To demonstrate the 3D nature of the Dirac cone in Na<sub>3</sub>Bi, it is necessary to show that the band dispersion is also linear along  $k_z$  (as well as  $k_x$  and  $k_y$ ), which was achieved by performing photon-energy-dependent ARPES measurements (27, 28). By assembling the measurements under a broad range of photon energies (27), we obtained the band structures of Na<sub>3</sub>Bi throughout the 3D BZ. Figure 3A illustrates the complete FS of Na<sub>3</sub>Bi in a 3D BZ, showing a pair of pointlike FSs in the vicinity of  $\Gamma$  at  $k_x = k_y = 0$

and  $k_{\pm} = \pm 0.095/\text{\AA}$  or  $\pm 0.29\pi/c$  (where  $c$  is the  $z$ -direction lattice constant), which agrees well with our ab initio calculations that predict two Dirac points at  $k_{\pm} = \pm 0.26\pi/c$  (15). In Fig. 3A (ii), which shows the data for a Na-deficient sample surface, an additional cylindrical FS appears and vertically crosses the whole 3D BZ (and thus is dispersionless along  $k_z$ ). This feature originates from the surface states (27, 28) that emerge due to the loss of the surface Na atoms, which easily migrate away during the experiment (27).

As well as studying the 3D FS, we investigate the band dispersion along all three  $k$  directions. Similar to Fig. 2C, Fig. 3B illustrates the 3D electronic structure along the  $k_y^D$ - $k_z^D$  direction, showing a clearly elongated (along the  $k_z^D$  direction) Dirac cone (corresponding to a much smaller  $V_z$ ; see Fig. 3, B and C). Furthermore, we study the detailed dispersions along each momentum direction (see schematics in Fig. 3, D to F): For a 3D Dirac fermion, ARPES measurements along any  $k$  direction should yield either

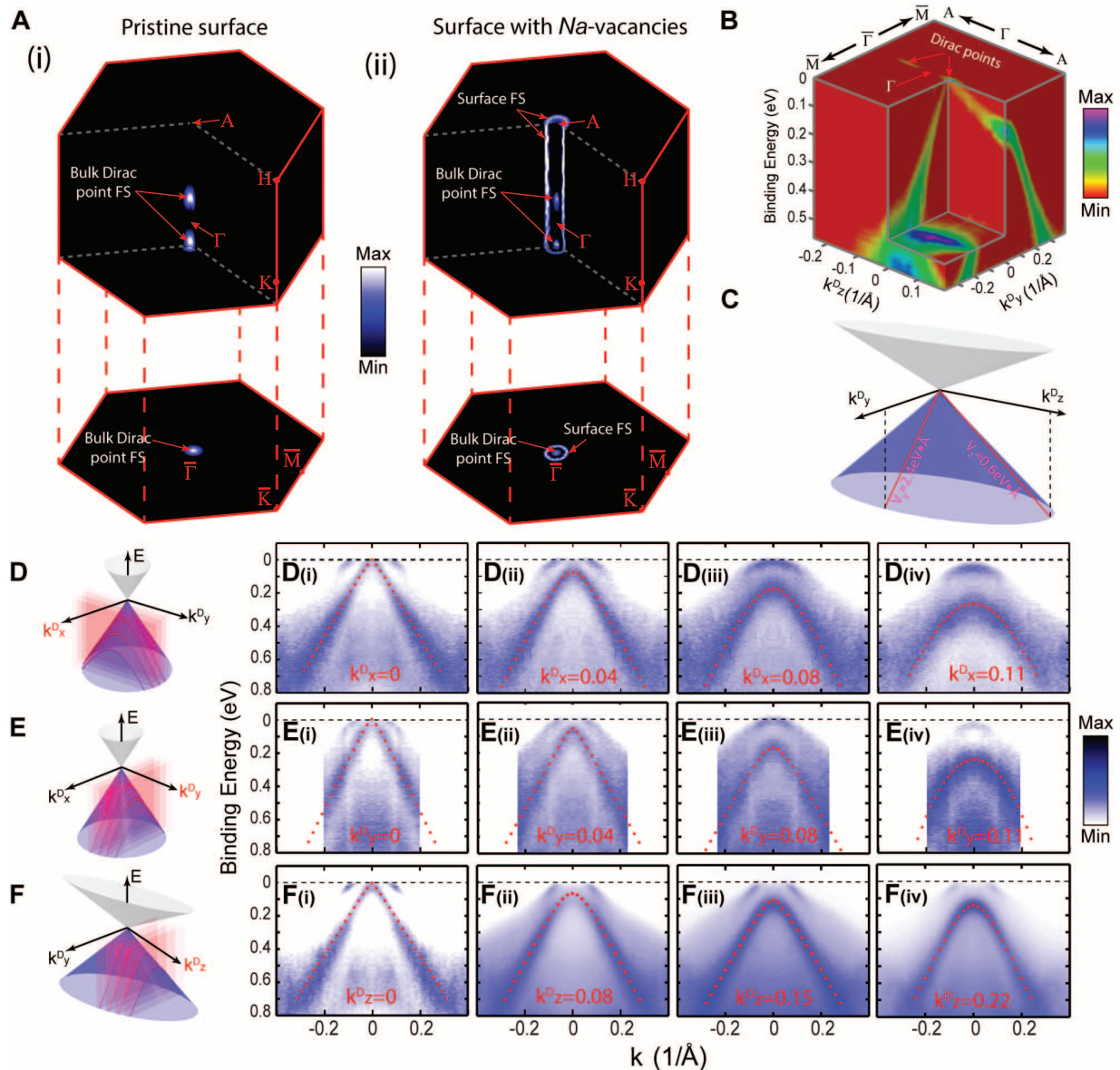


**Fig. 3. Dispersion of the 3D Dirac fermion along all three momentum directions.** (A) FS map across the whole 3D BZ (top panel) and its projection to the surface BZ (bottom panel) on (i) pristine and (ii) Na-deficient surfaces. An additional FS appears in panel (ii) [see text and (27) for details]. (B) A 3D intensity plot of the photoemission spectra (along the  $k_y^D$ - $k_z^D$  direction) shows the elongated (along the  $k_z^D$  direction) cone-shape dispersion, indicating the large anisotropy between the  $k_y$  and the  $k_z$  direction. (C) The schematic of the  $k_y^D$ - $k_z^D$  Dirac cone reconstructed from the experimental fit parameters:  $V_x = 2.4 \text{ eV}\cdot\text{\AA}$ , and  $V_z = 0.6 \text{ eV}\cdot\text{\AA}$  (27). (D to F) Schematics show the dispersions

(red curves) that slice through the 3D Dirac cones at different ( $k_x^D$ ,  $k_y^D$ , or  $k_z^D$ ) momentum locations, showing either a linear or a hyperbolic shape. The Dirac velocity parameters obtained from our experiments are  $V_x = 2.8 \text{ eV}\cdot\text{\AA}$ ,  $V_y = 2.4 \text{ eV}\cdot\text{\AA}$ , and  $V_z = 0.6 \text{ eV}\cdot\text{\AA}$  (27). (D) (i to iv) Measured dispersion at  $k_x^D = 0, 0.04, 0.08$ , and  $0.11 \text{ \AA}^{-1}$ , respectively. Red dotted lines show the fitted dispersions that agree well with the experiments [see text and (27)]. (E) (i to iv) Experiment and fitted dispersions at  $k_y^D = 0, 0.04, 0.08$ , and  $0.11 \text{ \AA}^{-1}$ , respectively. (F) (i to iv) Experiment and fitted dispersions at  $k_z^D = 0, 0.08, 0.15$ , and  $0.22 \text{ \AA}^{-1}$ , respectively.

linear or hyperbolic dispersions depending on whether the measurement cuts through the Dirac point. This is different from the usual parabolic dispersions of massive electrons.

In Fig. 3, D to F (i to iv), we use four examples along each  $k$  direction to show typical ARPES dispersions on  $\text{Na}_3\text{Bi}$  [for additional measurements and analysis, see (27)]. Along each  $k$  direction, the dispersion evolves from a linear [Fig. 3, D to F (i)] to a hyperbolic [Fig. 3, D to F (ii to iv)] shape, as expected. Notably, to fit all of the ARPES measurements [including those in (27)] requires only one set of 3D Dirac cone parameters ( $V_x = 2.75 \text{ eV}\cdot\text{\AA}$  or  $4.17 \times 10^5 \text{ m/s}$ ,  $V_y = 2.39 \text{ eV}\cdot\text{\AA}$  or  $3.63 \times 10^5 \text{ m/s}$ , and  $V_z = 0.6 \text{ eV}\cdot\text{\AA}$  or  $0.95 \times 10^5 \text{ m/s}$ ). This excellent agreement proves that the bulk band structure of  $\text{Na}_3\text{Bi}$  forms 3D Dirac cones, with a large anisotropy along the  $k_z$  direction ( $V_z \approx 0.25 V_x$ ; see Fig. 3C).

To test the robustness of 3D Dirac fermion in  $\text{Na}_3\text{Bi}$ , we modified the sample surface (by in situ evaporating K atoms; see Fig. 4, A and B) and monitored the band dispersions' evolution with the increase in surface impurities. In addition, the K doping can compensate the charge loss caused by the surface Na-atom loss discussed above [and in (27)]. Indeed, we could even

overcompensate the charge loss with sufficient doping and observed the upper part of the Dirac cone beyond the Dirac point (Fig. 4C). With the increase in K doping, the  $E_F$  shifts upward (Fig. 4, D to F), whereas the surface-state band disappears (Fig. 4, E and F), owing to the deterioration of the sample surface by randomly deposited K atoms. By contrast, the bulk Dirac cone (both the linear dispersion and the Dirac point) persists despite such surface deterioration (Fig. 4, E and F), supporting the notion that the Dirac fermion is protected by the bulk crystal symmetry (which is preserved during surface K doping).

The TDS  $\text{Na}_3\text{Bi}$  realizes a 3D counterpart of graphene, opening the door to exploring other 3D TDSs, some of which may realize various exciting applications of graphene in 3D materials. Furthermore, the extremely long Fermi wavelength (which diverges at the Dirac points) of the bulk conducting electrons in a TDS can greatly enhance the Ruderman-Kittel-Kasuya-Yosida interaction, making it possible to realize ferromagnetic states by unusually dilute magnetic doping [similar to the Dirac surface states in a topological insulator (29)]—which could make the TDS an ideal platform for spintronics applications.

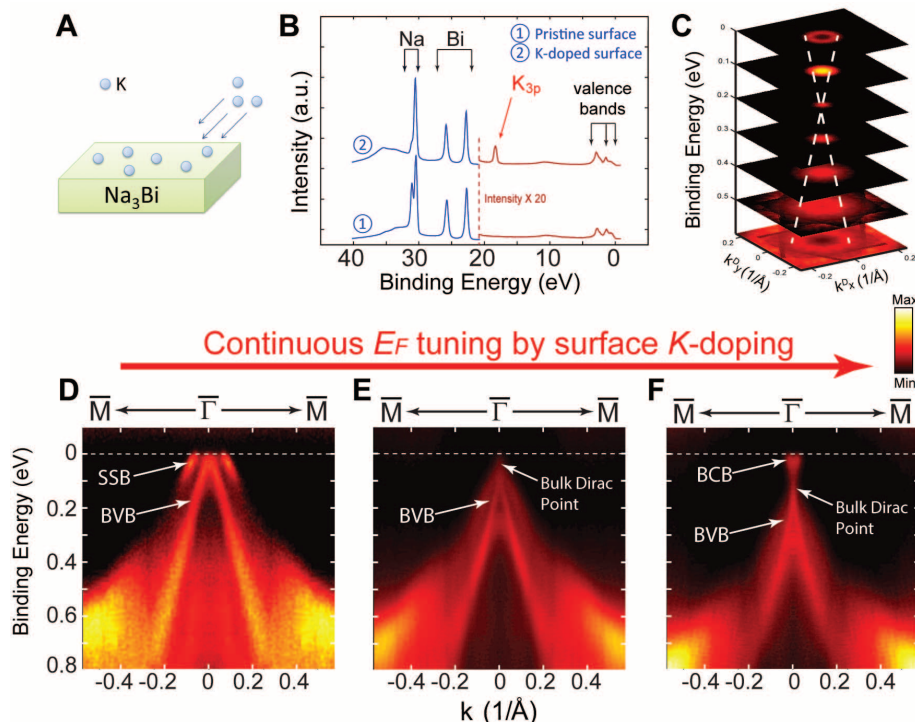


**Fig. 4. Bulk Dirac fermion stability and  $E_F$  tuning by surface doping.** (A) Illustration of the in situ surface K doping. (B) Core-level photoemission spectra before and after the K doping show the  $K_{3p}$  core-level peak (which can be used to monitor the dosage level). (C) Stacking plot of constant-energy contours shows the upper Dirac cone after the in situ K doping. White dashed lines are guides to the eye that trace the Dirac dispersions. (D to F) ARPES intensity plots show the rise in  $E_F$  with K dosage: (D) before in situ K doping; (E) at a level of K doping required to bring  $E_F$  to the bulk Dirac point; and (F) after further K doping drives the system into n-type. The surface state band (SSB) in (D) is destroyed by the K doping and thus does not appear in (E) and (F). BCB, bulk conduction band; BVB, bulk valence band.

## References and Notes

1. A. K. Geim, K. S. Novoselov, *Nat. Mater.* **6**, 183–191 (2007).
2. A. H. Castro Neto, F. Guinea, N. M. R. Peres, K. S. Novoselov, A. K. Geim, *Rev. Mod. Phys.* **81**, 109–162 (2009).
3. M. Z. Hasan, C. L. Kane, *Rev. Mod. Phys.* **82**, 3045–3067 (2010).
4. X.-L. Qi, S.-C. Zhang, *Rev. Mod. Phys.* **83**, 1057–1110 (2011).
5. K. S. Novoselov *et al.*, *Science* **306**, 666–669 (2004).
6. C. L. Kane, E. J. Mele, *Phys. Rev. Lett.* **95**, 226801 (2005).
7. L. Fu, C. L. Kane, E. J. Mele, *Phys. Rev. Lett.* **98**, 106803 (2007).
8. J. E. Moore, *Nature* **464**, 194–198 (2010).
9. C. Herring, *Phys. Rev.* **52**, 365–373 (1937).
10. S. Murakami, *New J. Phys.* **9**, 356 (2007).
11. G. E. Volovik, in *Quantum Analogues: From Phase Transitions to Black Holes and Cosmology*, W. Unruh, R. Schützhold, Eds., Lecture Notes in Physics (Springer, Berlin, Heidelberg, 2007), vol. 718, pp. 31–73.
12. X. Wan, A. M. Turner, A. Vishwanath, S. Y. Savrasov, *Phys. Rev. B* **83**, 205101 (2011).
13. A. A. Burkov, L. Balents, *Phys. Rev. Lett.* **107**, 127205 (2011).
14. S. M. Young *et al.*, *Phys. Rev. Lett.* **108**, 140405 (2012).
15. Z. Wang *et al.*, *Phys. Rev. B* **85**, 195320 (2012).
16. P. Goswami, S. Chakravarty, *Phys. Rev. Lett.* **107**, 196803 (2011).
17. A. K. Geim, *Science* **324**, 1530–1534 (2009).
18. M. Koshino, T. Ando, *Phys. Rev. B* **81**, 195431 (2010).
19. E. Röber, K. Hackstein, H. Coufal, S. Sotier, *Phys. Status Solidi B* **93**, K99–K102 (1979).
20. A. A. Abrikosov, *Phys. Rev. B* **58**, 2788–2794 (1998).
21. W. Zhang *et al.*, *Phys. Rev. Lett.* **106**, 156808 (2011).
22. C.-X. Liu *et al.*, *Phys. Rev. B* **81**, 041307 (2010).
23. G. E. Volovik, *The Universe in a Helium Droplet* (Clarendon, Oxford, 2003).
24. G. Xu, H. Weng, Z. Wang, X. Dai, Z. Fang, *Phys. Rev. Lett.* **107**, 186806 (2011).
25. K.-Y. Yang, Y.-M. Lu, Y. Ran, *Phys. Rev. B* **84**, 075129 (2011).
26. F. R. Klinkhamer, G. E. Volovik, *Int. J. Mod. Phys. A* **20**, 2795–2812 (2005).
27. Materials and methods are available as supporting materials on Science Online.
28. Y. Chen, *Front. Phys.* **7**, 175–192 (2012).
29. Q. Liu, C.-X. Liu, C. Xu, X.-L. Qi, S.-C. Zhang, *Phys. Rev. Lett.* **102**, 156603 (2009).

**Acknowledgments:** We thank X. L. Qi and Z. Wang for insightful discussions, S. Clarke and J. Wright for help in sample synthesis, and P. Han and R. Yang for help with data analysis. Y.L.C. and B.Z. acknowledge support from the Engineering and Physical Sciences Research Council (UK) grant EP/K04074X/1 and a Defense Advanced Research Projects Agency (USA) MESA project (no. N66001-11-1-4105). Z.K.L. and Z.X.S. acknowledge support by the U.S. Department of Energy, Office of Science, Materials Sciences and Engineering Division. Z.F., X.D., and H.M.W. acknowledge support by the NSF of China, the National Basic Research Program of China, and the International Science and Technology Cooperation Program of China. The experiments were performed, and data were collected, at Beamline 10.0.1 of the Advanced Light Source, Lawrence Berkeley National Laboratory, USA.

## Supplementary Materials

www.sciencemag.org/content/343/6173/864/suppl/DC1  
Materials and Methods  
Figs. S1 to S8  
References (30–38)

23 August 2013; accepted 2 January 2014  
Published online 16 January 2014;  
10.1126/science.1245085